Plasmonics
https://doi.org/10.1007/s11468-020-01323-3

# Plasmonic Antenna Embedded Chalcogenide MZI Circuit for Ultra-high Density Up- and Downlink Transmission

**Arumona Edward Arumona[1,2,3] · Anita Garhwal[4] · Montree Bunruangses[5] · Kanad Ray[6] · Phichai Youplao[7] · Suphanchai Punthawanunt[8] · Preecha Yupapin[1,2]**

Received: 10 August 2020 / Accepted: 3 November 2020


**Abstract**
A unique device is proposed for ultra-high density up- and downlink transmission. The device comprises of the chalcogenide Mach–Zehnder interferometer (MZI) and panda ring resonator with silver bars at the center microring at the upper and lower parts of the MZI. The device is operative based on the space–time function where the input space (soliton) via the input port multiplexes with time at the add port of the device with a wavelength bandwidth of 1.50–3.50 μm and the frequency bandwidth of 85–250 THz. The WGM is observed at the upper (uplink) and lower (downlink) center microring with suitable parameters. The silver bars at the center microring form the dipole oscillation, where the uplink and downlink plasmonic antennas have the directivity 18.68 and 13.27, and gain is 9.34 and 6.64, respectively. The light fidelity (LiFi uplink and downlink) employs the wavelength spectrum while the wireless fidelity (WiFi uplink and downlink) employs the frequency spectrum. The LiFi uplink and downlink have an optimum wavelength of 2.30 μm and 2.27 μm, respectively, while the WiFi uplink and downlink have an optimum frequency of 130 THz and 132 THz. For the transmission signal, the bit rate of 28 $Pbits^{-1}$ is achieved. The bit error rate (BER) value of 0.36 is obtained which indicates the system performance. Low BER value indicates high system performance. The device can be employed for the coverage of the light-wave and microwave wavelength link for 6G communication, where AI (artificial intelligence), 3D communication, code encryption, and secured transmission can be applied.

**Keywords** Plasmonic antenna · Spin-wave transmission · Mach–Zehnder · High-density flip-flop · 6G communication

## Introduction

Communication involves sending information over various network channels, where the information transmission varies depending on the channel capacity. The greater the speed of transmitting this information, the better the communication and wide application in human life. There are different types of networks such as the cellular networks (1G, 2G, 3G, 4G, and 5G) which transmit information. In the last 10 years, the 4G network is commercialized where the speed of transmitting information has greatly improved with wide application in various aspects of human life.

✉ Preecha Yupapin
preecha.yupapin@tdtu.edu.vn

[1] Computational Optics Research Group, Advanced Institute of Materials Science, Ton Duc Thang University, District 7, Ho Chi Minh City, Vietnam

[2] Faculty of Applied Sciences, Ton Duc Thang University, District 7, Ho Chi Minh City, Vietnam

[3] Division of Computational Physics, Institute for Computational Science, Ton Duc Thang University, Ho Chi Minh City 700000, Vietnam

[4] Amity School of Engineering & Technology, Amity University Rajasthan, Jaipur, India

[5] Department of Computer Engineering, Faculty of Industrial Education, Rajamangala University of Technology Phra Nakhon, Bangkok 10300, Thailand

[6] Amity School of Applied Sciences, Amity University Rajasthan, Jaipur, India

[7] Department of Electrical Engineering, Faculty of Industry and Technology, Rajamangala University of Technology Isan Sakon Nakhon Campus, Sakon Nakhon 47160, Thailand

[8] Faculty of Science and Technology, Kasem Bundit University, Bangkok 10250, Thailand

Published online: 12 January 2021

Recently, the 5G network has been commercialized with an increase in the speed of transmitting information and very wide applications. The 5G network has led to the establishment of smart technologies where big data plays a big role. There is always a need to constantly develop the kind of network used in transmitting the information. The better the network in terms of the bandwidth, the wider the application in various aspects of human life. The 6G network is an active area of research where it is expected that the bandwidth will be increased and also increase the area of application as compared to the 5G network. The 5G network has a maximum bit rate of 35.46 Gbps while the 6G network is expected to have 100 Gbps and beyond [1–9]. Chen et al. [10] surveyed the importance of a 6G network over the 5G network highlighting the improvement in the area of application. The 6G network can be employed as a pervasive intelligent system. Lu and Zheng [11] surveyed the intended impact of the 6G network on various aspects of human life. The study also proposes some definitions and applications of the 6G network as well as the architecture. Wang et al. [12] surveyed the possible security and privacy issues that are involved in the 6G network. The 6G network has the potential to be the network that will drive the AI system to the next level where it will have a massive impact on human everyday life. The security and privacy issues such as communication, access control, and authentication are discussed in the study. Encryption and malicious behavior are also security and privacy issues that are also discussed in the study. Manogaran et al. [13] proposed a security measure that can be employed in a 6G network environment. The security measure that is integrated and based on block-chain is proposed to curtail the security and privacy issues that will arise in the 6G network environment. Ma et al. designed a 6G communication device. The device is an indoor terahertz communication device. The device consists of an intelligent reflecting surface (IRS) that is intended to improve indoor communication in the terahertz region of 0.1–10 THz. Khan et al. [14] proposed a power technique that will improve the performance of a multi-access system that is employed for the internet of things. The multiple access system employed in the study is the non-orthogonal multiple access. The power method employed did not affect the quality of service. Adeogun et al. [15] proposed a wireless 6G communication network system. The wireless system is based on isochronous real-time. The 6G wireless network system has a short range. The proposed wireless network can be employed in industry as production modules as well as robots. In this work, a chalcogenide MZI circuit is proposed for ultra-high density up- and downlink transmission. The chalcogenide MZI circuit has two panda ring resonators at the upper and lower arms. The silver metamaterial is embedded at the center microring which forms the plasmonic antenna. The plasmonic antenna can control light and have strong confinement where its tunability is high, making it suitable for terahertz applications [16]. This work aims to improve the operation bandwidth for 6G communication, where the transmission bandwidth and modes are the targets. The chalcogenide material is used as the MZI material because of its broad transmission bandwidth and has an ultra-wavelength range of 1–10 µm [17]. The resonant results of the integrated circuit are obtained, which is suitable for the connection between light (LiFi) and microwave (WiFi) wavelength region. The proposed circuit offers the advantage to be applied for 6G communication. The simulation of the system involves the Optiwave program where the whispering gallery mode (WGM) [18, 19] which is employed for wireless communication is observed at the center microring while the Matlab program employing the parameters extracted from the Optiwave simulation is used to plot the graphs and obtain other results.

## Theoretical Background

Using the Drude model [20, 21], the electric dipole oscillation excited by the silver bars can be achieved. The silver bars are embedded at the center microring with the Mach–Zehnder interferometer, which forms the communication device, as shown in Fig. 1.

$$\epsilon(\omega) = 1 - \frac{ne^2}{\epsilon_0 m\omega^2} \tag{1}$$

where $n$ is known as the electron density, $m$ is known as the mass, $\omega$ is known as the angular frequency, $\epsilon_0$ is known as the relative permittivity, and $\varepsilon$ is known as the electron charge. The plasma frequency ($\omega_p$) at the resonance is obtained from the angular frequency, which is given by an Eq. (2).

$$\omega_p = \left[\frac{ne^2}{\epsilon_0 m}\right]^{-1/2} \tag{2}$$

the electron density becomes $n = \frac{\omega_{pe_0m}^2}{e^2}$ from Eq. (2).

The space–time modulation function is given as [22]:

$$Be^{-i(\omega t + \frac{E_n}{n\hbar}t)} \tag{3}$$

where the input dark soliton is $B = \bar{B}.Tanh\left(\frac{T}{T_0}\right)\exp\left(\frac{z}{2L_D}\right)$, $e^{i\omega t}$ is the time function, $\omega t$ is the phase term, and $\frac{E_n}{n\hbar}$, $n$ = 1,2,3,... the spin number is $\pm\frac{\hbar}{2}$, spin-up matrix$\frac{\hbar}{2}\begin{vmatrix} 0 & -i \\ i & 0 \end{vmatrix}$, spin-down matrix$\frac{\hbar}{2}\begin{vmatrix} 0 & 1 \\ 1 & 0 \end{vmatrix}$, $\hbar$ is the reduced

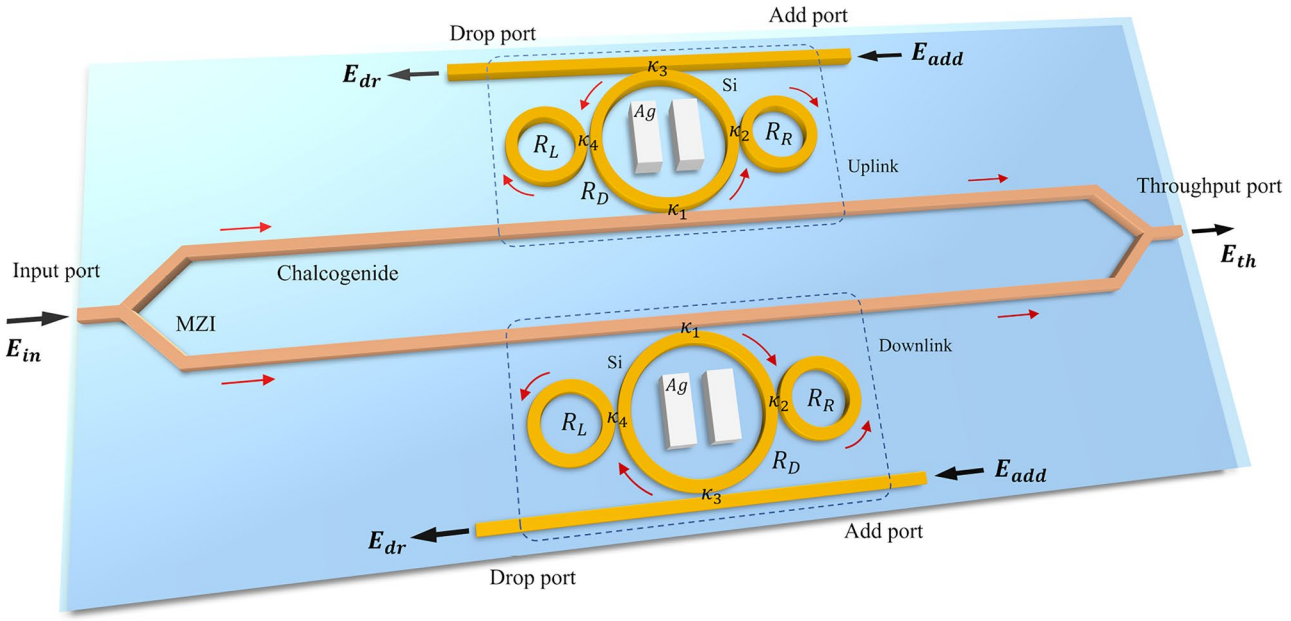


**Fig. 1** The microring plasmonic circuits, where $E_{in}$, $E_{add}$, $E_d$, and $E_{th}$ are input, add, drop, and throughput ports, respectively. Ag: silver bars, Si: silicon, PD; R, $R_R$, $R_L$ are defined as the center ring radius, and two side ring radii, respectively. $K_R$, $K_L$ are defined as the coupling constants

Planck's constant, where $\hbar = \frac{h}{2\pi}$, and $h$ is the Planck's constant. $\bar{B}$ and $z$ are the soliton amplitude and propagation distance. $T$ is the propagation time of the soliton, $L_D = \frac{T_0^2}{\beta}$, where $T_0$ is the initial propagation time. $\beta$ is the propagation constant. The MZI output [23] is given in Eq. (4) and the output is normalized as given in Eqs. (5) and (6).

$$I = I_1 + I_2 + 2\sqrt{I_1 I_2} Cos\varphi \tag{4}$$

where $\varphi = \frac{2\pi \Delta n_{eff}}{\lambda} L$, $L$ is the length of the stack layer, $n_{eff}$ is the effective refractive index, and $\lambda$ is the wavelength. $I$, $I_1$, $I_2$ defined as the intensities.

$$\frac{I_{th}}{I_{in}} = \left[\frac{E_{th}}{E_{in}}\right]^2 \tag{5}$$

$$\frac{I_{drop}}{I_{in}} = \left[\frac{E_{drop}}{E_{in}}\right]^2 \tag{6}$$

The communication device consists of the MZI which divides the input soliton into two equal parts. The MZI functions as a 50:50 coupler. The two panda rings are attached to the MZI and act as the upper and lower parts. The center microring has two small rings. The input port is labelled as $E_{in}$, the output of the communication device are the drop port and throughput port labelled as $E_{dr}$, and $E_{th}$ while the add port is labelled as $E_{add}$ which acts as the port for modulation or multiplexing. The silver bars at the center microring are metamaterials which can form the metamaterial antenna as explained in [24].

## Results and Discussion

The communication device is designed with the Optiwave program (OptiFDTD) [25] where the mesh cell size of 218, 41, 861 ($x$, $y$, and $z$ axes, respectively) is employed with the automatic implementation of the grid size by the program. The MZI is a chalcogenide material ($AS_2Se_3$) having the refractive index of 2.818, and the panda ring structure at the upper and lower parts of MZI is silicon material. The optimized parameters in this work are the realistic parameters that can be employed for the fabrication of the proposed circuit in Table 1. The WGM modes and spin waves are formed when the two-side rings are controlled when light travels around the center microrings with the optimized parameters. The polaritons are the electrons excited by plasmonic waves in the form of WGMs. The spin-waves are formed by the polarized electrons excited by the silver bars, where the transmission is formed by the dipole oscillation. The two side rings are known as the phase modulators, which induced the nonlinearity into the center ring. The

**Table 1** The optimized simulation parameters

| Parameters | Symbols | Values | Units |
|---|---|---|---|
| Input power | $P$ | 100–500 | mW |
| Silicon center ring radius | $R$ | 2.0 | μm |
| MZI length | $L$ | 60 | μm |
| Si-small ring radius | $R_L$ | 0.8 | μm |
| Si-small ring radius | $R_R$ | 0.8 | μm |
| Dielectric constant Ag | $\in_r$ | 1.0 | |
| Silver thickness | $d$ | 0.1 | μm |
| Silver length | $L$ | 0.5 | μm |
| refractive index of silver [32] | $n_{Ag}$ | 0.14 | |
| Insertion loss | $\gamma$ | 0.01 | |
| Chalcogenide refractive index [33] | $n_{chg}$ | 2.818 | |
| Coupling coefficient | $\kappa$ | 0.50–0.70 | |
| Refractive index Si [30] | $n_{Si}$ | 3.42 | |
| Si nonlinear refractive index [34] | $n_2$ | $1.3 \times 10^{-13}$ | $m^2\ W^{-1}$ |
| Wavelength bandwidth | $\lambda_1$ | 1.50–3.50 | μm |
| Waveguide core effective [34] | $A_{eff}$ | 0.30 | $\mu m^2$ |
| Waveguide loss | $\alpha$ | 0.50 | $dB.(cm)^{-1}$ |
| Plasma frequency [35] | $\omega_p$ | $1.2990 \times 10^{16}$ | rad $s^{-1}$ |
| Electron mass | $m$ | $9.11 \times 10^{-31}$ | kg |
| Electron charge | $e$ | $1.6 \times 10^{-19}$ | Coulomb |
| Permittivity of free space | $\varepsilon_o$ | $8.85 \times 10^{-12}$ | $Fm^{-1}$ |

nonlinearity makes the observation of the WGM possible when the input light enters the system through the input port. The WGM results from the light been trapped within the center ring due to the nonlinearity. The wavelength bandwidth in this work is in the range of 1.50–3.50 μm, and the frequency bandwidth is in the range of 85–250 THz. The simulation model boundary condition employed is the anisotropic perfect matched layer. The time-step of 20,000 is applied to obtain resonant results. The space–time function as given in Eq. (3) results from the input soliton multiplexing with time at the add port which excites the silver bars at the center ring and the behavior of the electron in the silver bars is described by Eq. (1). At the output of the system, normalization is applied as given in Eqs. (5) and (6). The WGM is observed at the upper and lower center rings after the simulation of 20,000 time-steps with the appropriate parameters as given in Table 1. The WGM results are shown in Fig. 2. Figure 2 a is the WGM result at the upper center ring, where the uplink and downlink can perform in either light or antenna operation. Figure 2 b shows the flow of plasmons within the device. The WGM formed at the two center rings is employed for LiFi and WiFi communication network. The LiFi is employed in the wavelength spectrum while the WiFi is employed in the frequency spectrum. The LiFi bandwidth is in the range of 1.50–3.50 μm while the WiFi bandwidth is in the range of 85–250 THz. The output signals are plotted by the Matlab program employing the parameters taken from the results of the OptiFDTD simulation. Figure 3 shows the output signals at the drop ports (upper and lower), throughput port, uplink, and downlink. The intensity at the throughput port is much higher than the other output ports. The throughput port forms the transmission signals where the signals been transmitted using the spin-wave. The output signals are plotted in the wavelength and frequency domains where broad spectral range and bandwidth are obtained, which are available for high capacity and security transmission for LiFi and WiFi links, respectively. The silver bars at the center microring forms the plasmonic antenna and the antenna profile is shown in Fig. 4. Figure 4 a and b is the uplink and downlink directivity. The directivity is dimensionless because no specific direction is considered as explained in [26]. The uplink directivity of 18.68 is higher than the downlink directivity of 13.27. Figure 4 c is the gain of the antenna where the optimum uplink gain is 9.34 and the optimum downlink gain is 6.64 when the input power is varied from 100 to 500 mW. The gain is directly proportional to the input power. The higher the input power the higher is the gain. The change in output gain can be applied for sensing applications, where the electro-optic sensors can be applied, where the sensor network can be linked, and real-time monitored and controlled. The LiFi and WiFi spectra are plotted in Fig. 5. Figure 5 a is the LiFi downlink and uplink. The downlink has a peak wavelength of 2.27 μm while the uplink has a peak wavelength of 2.30 μm. Figure 5 b is the WiFi downlink and uplink. The downlink has a peak frequency of 132 THz while the uplink has a peak frequency of 130 THz. The coverage wavelength and bandwidth are available for light and microwave transmission links, where the large bandwidth and spectral range are suitable for 6G communication. The spin waves of the uplink and downlink are plotted in Fig. 6 a and b.

Figure 6 a is the spin-wave plot of the LiFi uplink and downlink which are entangled zoomed from 2.40 to 3.00 μm for clarity while Fig. 6b is the spin-wave plot of the WiFi uplink and downlink which are entangled zoomed from 90 to 120 THz for clarity. The entanglement plot of the transmission signal is shown in Fig. 6c, d for the uplink and downlink where the flip-flop outputs have been obtained from the test nodes, which can be configured as the entanglement of quantum code transmission. Figure 6 e–f is the MZI output for the uplink and downlink where the spin projection is applied and at the throughput port, the spin is projected upwards to form the spin-up electrons while at the drop port, the spin is projected

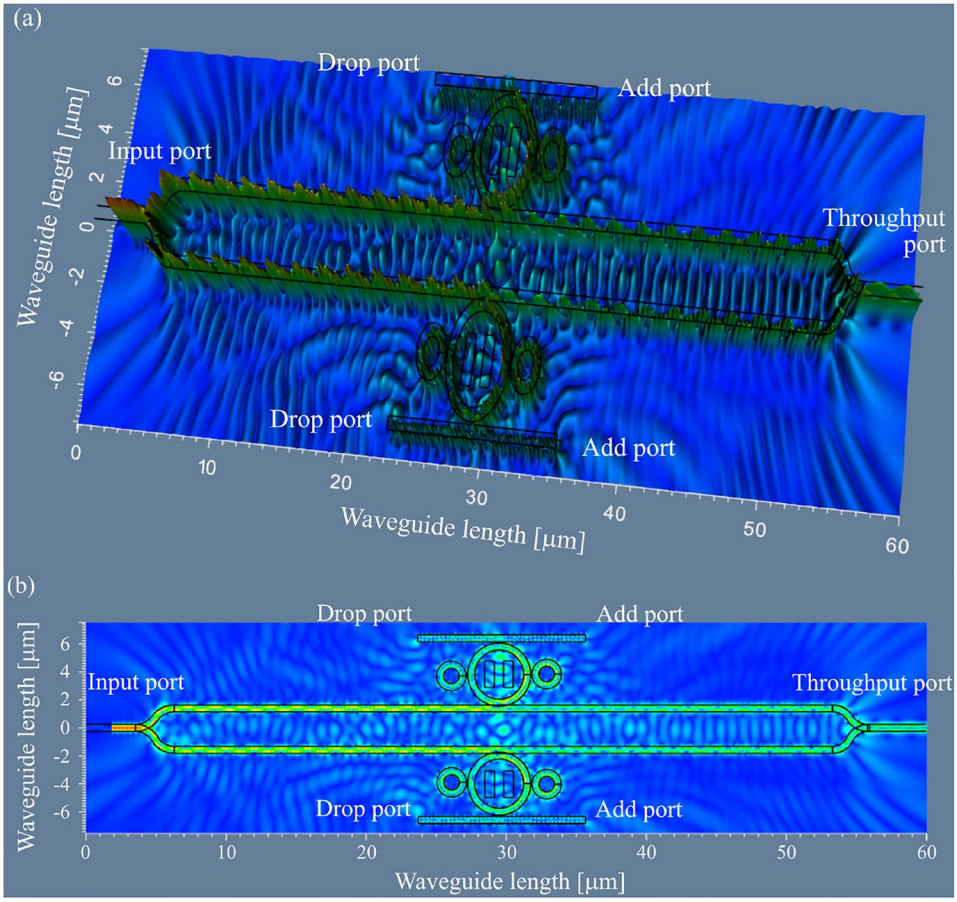


**Fig. 2** Graphical results of the multi-access system. **a** The WGMs are observed at the upper and lower center microring with the appropriate parameters in Table 1. **b** The flow of plasmons within the device

downwards to form the spin-down electrons. The electron spin results from the electron density that is formed by the oscillation of the electron cloud when the silver bars at the center ring are excited by the input space source (light). At the transmission port, the transmitted signal has a bit rate of 28 Pbits$^{-1}$ as shown in Fig. 7. The time sequence QCA (quantum cellular automata) [27] is applied in distinguishing the electron spins (spin-up and spin-down). The higher bit rates can be obtained by increasing the number of up- and downlink antennas and more multiplexed input signals. The simulation is validated by testing the transmission between up and downlink, where the bit error rate is obtained and plotted. The BER value shows the effectiveness of a system and the capability of the system in transmitting signals or information. Figure 8 is the BER plot of the communication system where the AGWN communication channel (additive Gaussian white noise) is employed as explained in [28]. The BER value

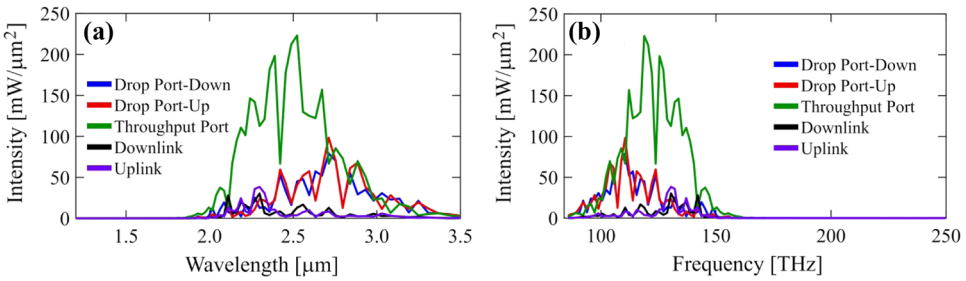


**Fig. 3** Plot of output signals with the uplink and downlink in the **a** wavelength domain and **b** frequency domain. Broad spectral range and bandwidth are obtained, which are available for high capacity and security transmission. Besides, the link between light and microwave is available using LiFi and WiFi links, respectively

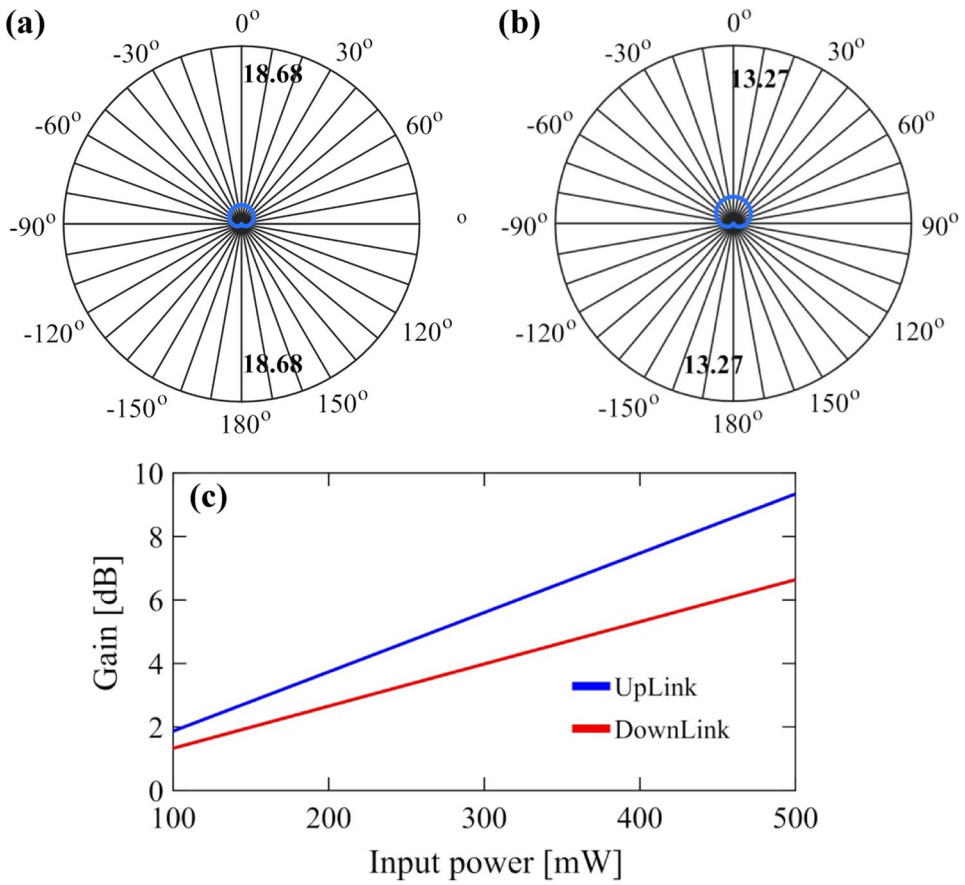


**Fig. 4** Plot of the plasmonic antenna outputs. **a**, **b** Uplink and downlink directivity. **c** Uplink and downlink gain. The change in output gain can be applied for sensing applications. The electro-optic sensors can be applied, in which the sensor network can be linked and real-time monitored and controlled

of 0.36 is obtained. The lower the BER value, the higher the system performance and vice versa. From Fig. 1, more nodes can be applied for big data transmission where the transmission signal at the throughput port can be multiplexed to obtain bit rates of 40 $Pbits^{-1}$ and more [28]. It can be applied for 3D and quantum transmission as well as for brain sensors [29, 30]. It can also be applied for security networks and surveillance systems [31]. The achieved frequency bandwidth in this work is ranged between 85 and 250 THz, which is compared to [3] and [37], achieved 0.1–10 THz and 0.06–10 THz, respectively. The advantages of optical solution over rf (radiofrequency) are as follows: the frequency spectrum (THz) is higher, the security of data transmission is higher, the power consumption is low, the data rate is higher and more advantages as explained in [36].

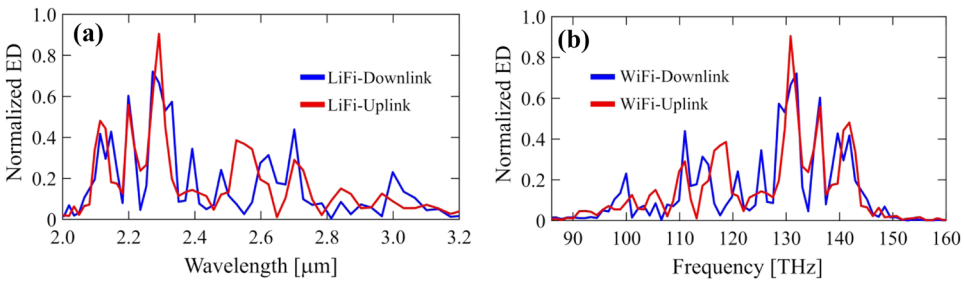


**Fig. 5** The plot of the LiFi uplink and downlink of the system are shown in Fig. 1. **a** A peak wavelength at 2.30 μm and 2.27 μm. **b** A peak frequency at 130 THz and 132 THz, where the coverage wavelength and bandwidth are available for light and microwave transmission links, and the large bandwidth and spectral range are suitable for 6G communication

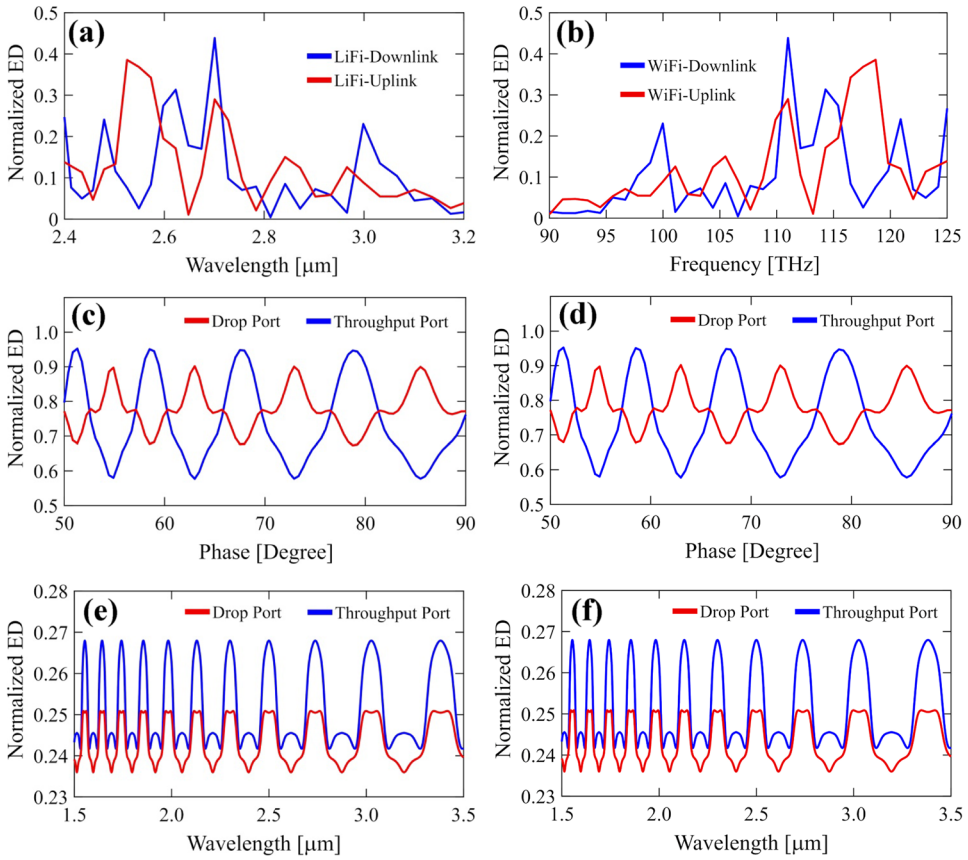


**Fig. 6** The spin-wave outputs for both **a**, **b** LiFi and WiFi uplink and downlink, respectively. **c**, **d** The flip-flop outputs obtained from the test nodes, which can be configured as the entanglement of quantum code transmission. **e**, **f** The MZI output for the uplink and downlink

## Conclusion

A plasmonic antenna circuit of ultra-high density is proposed for up- and downlink transmission. The plasmonic antenna circuit consists of the chalcogenide MZI and two panda rings (upper and lower) with silver bars at the center microring, which form the uplink and downlink plasmonic antenna. The proposed device has a wavelength bandwidth of 1.50–3.50 μm while the frequency bandwidth is in the range of 85–250 THz. The uplink and downlink antennas have a directivity of 18.68 and 13.27, respectively. The uplink and downlink antenna gains are 9.34 and 6.64, respectively. The LiFi uplink and downlink have peak wavelengths of 2.30 μm and 2.27 μm, respectively, while the WiFi uplink and downlink have peak frequencies of 130 THz and 132 THz, respectively. The bit rate of 28 $Pbits^{-1}$ is achieved. The BER value of 0.36 is obtained. In application, the device can be employed for 6G communication, quantum transmission, big data analytics, and information encryption.

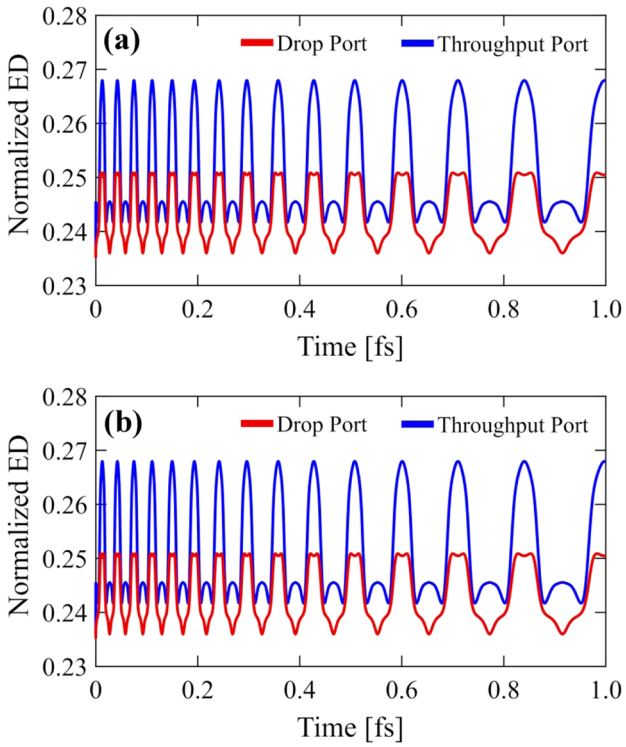


**Fig. 7** The plot of the transmission signals **a** uplink and **b** downlink with a bit rate of 28 Pbits$^{-1}$ is obtained, where the higher bit rates can be obtained by increasing the number of up- and downlink antennas and more multiplexed input signals

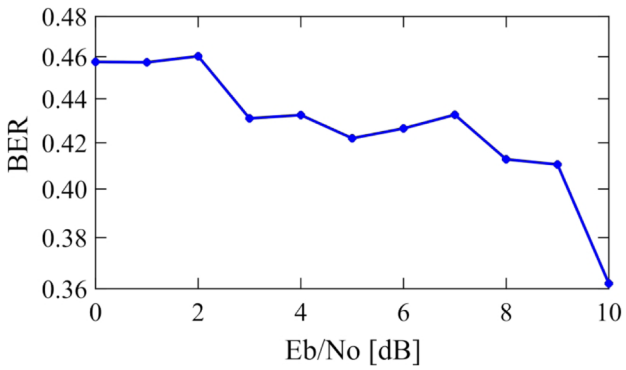


**Fig. 8** The plot of the test bit error rate between the up- and downlink nodes where the BER value of 0.36 has been obtained, which is acceptable for transmission

**Acknowledgements** One of theauthors (Mr. Arumona) would like to thank the Ton DucThang University, Vietnamfor their financial support. Thisresearch is funded by the Foundation of Science and Technology Development ofTon Duc Thang University (FOSTECT), website: http://fostect.tdtu.edu.vn, under theresearch grant number FOSTECT.2017.BR.07.

**Authors Contributions** Arumona Edward Arumona: simulation, analyzed, writing and revision; Anita Garhwal: graphic improvement and discussion; Montree Bunruangses: Matlab results improvement and discussion; Kanad Ray: discussion and premium quality improvement; Phichai Youplao: comparing Optiwave and Matlab results, and discussion; Suphanchai Punthawanunt: discussion and English polishing; Preecha Yupapin: modeled, analyzed, discussion, final editing and submission. All authors have read through the manuscript.

**Funding** This research is funded by the Foundation of Science and Technology Development of Ton Duc Thang University (FOSTECT), website: https://fostect.tdtu.edu.vn, under the research grant number FOSTECT.2017.BR.07.

## Compliance with Ethical Standards

**Consent to Participate** All authors are pleased to publish in this article.

**Consent to Publish** All authors are welcome to publish this article.

**Competing Interests** The authors declare that they have no conflict of interest.

## References

1. Dang S, Amin O, Shihada B, Alouini MS (2020) What should 6G be. Nature Electronics 3:20–29
2. Zhou Y et al (2020) "Service aware 6G: An intelligent and open network based on convergence of communication, computing and caching". Digital Communications and Networks. 1–9
3. Ma X et al (2020) Intelligent reflecting surface enhanced indoor terahertz communication systems. Nano Communication Networks 24(100284):1–33
4. Jiang T et al (2020) "6G perspectives: techniques and challenges". Digital Communications and Networks
5. Alsharif MH, Kelechi AH, Albreem MA, Chaudhry SA, Zia MS, Kim S (2020) Sixth generation (6G) wireless networks: Vision, research activities, challenges and potential solutions. Symmetry 12(4):1–21
6. Sergiou C, Lestas M, Antoniou P, Liaskos C, Pitsillides A (2020) Complex systems: A communication network perspective toward 6G. IEEE Access 8:89007–89030
7. Viswanathan H, Mogensen PE (2020) Communication in the 6G era. IEEE Access 8:57063–57074
8. Huang T, Yang W, WU J, MA J, Zhang X, Zhang D (2019) A survey on green 6G network: Architecture and technologies. IEEE Access 7:175758–175768
9. Rappaport TS et al (2019) Wireless communications and applications above 100 GHz: Opportunities and challenges for 6G and beyond. IEEE Access 7:78729–78759
10. Chen Y, Liu W, Niu Z, Feng Z, Hu Q, Jiang T (2020) "Pervasive intelligent endogenous 6G wireless systems: Prospects, theories and key technologies". Digital Communications and Networks. 1–14
11. Lu Y, Zheng X (2020) 6G: A survey on technologies, scenarios, challenges, and the related Issues. Journal of Industrial Information Integration 19(100158):1–51
12. Wang M, Zhu T, Zhang T, Zhang J, Yu S, Zhou W (2020) "Security and privacy in 6G networks: New areas and new challenges". Digital Communications and Networks. 1–16

13. Manogaran G et al (2020) "Blockchain based integrated security measure for reliable service delegation in 6G communication environment". Computer Communications. 1–20
14. Khan WU, Jameel F, Jamshed MA, Pervaiz H, Khan S, Liu J (2020) Efficient power allocation for NOMA-enabled IoT networks in 6G era. Physical Communication 39(101043):1–10
15. Adeogun R, Berardinelli G, Mogensen PE, Rodriguez I, Razzaghpour M (2020) Towards 6G in X-subnetworks with sub-millisecond communication cycles and extreme reliability. IEEE Access 8:110172–110188
16. Dash S, Patnaik A "Performance of graphene plasmonic antenna in comparison with their counterparts for low-terahertz applications". Plasmonics.13, 2353–2360
17. Kalraa S et al (2020) Investigation of $As_2S_3$-borosilicate chalcogenide glass-based dispersion-engineerd photonic crystal fibre for broadband supercontinuum generation in the mid-IR region. J Mod Opt 67(10):920–926
18. Punthawanunt S, Aziz MS, Phatharacorn P, Chiangga S, Ali J, Yupapin P (2018) LiFi cross-connection node model using whispering gallery mode of light in a microringresonator. Microsyst Technol 24(12):4833–4838
19. Chaiwong K, Bahadorun M, Amiri IS, Youplao P, Pornsuwancharoen N, Yupapin P (2018) Electric-optic conversion circuit incorporating a fiber optic loop for light fidelity up-down link use. Microwave and Optical Technology Letters 61(2):526–531
20. Tunsiri S, Thammawongsa N, Threepak T, Mitatha S, Yupapin P (2019) Microring switching control using plasmonic ring resonator circuits for super-channel use. Plasmonics 14:1669–1677
21. Schuller JA, Barnard ES, Cai W, Jun YC, White JS, Brongersma ML (2010) Plasmonics for extreme light concentration and manipulation. Nature Mater 9:193–204
22. Agrawal GP (2011) "Nonlinear fiber optics: its history and recent progress", [invited]. Journal of Optical Society America B 28(12):A1–A10
23. Sarapat N et al (2019) LiFi up-downlink conversion node model generated by inline successive optical pumping. Microsyst Technol 25:945–950
24. Arumona AE, Garhal A, Punthawanunt S, Ray K, Youplao P, Yupapin P ( 2020) "Micro-metamaterial antenna characteristics using microring embedded silver bars". Microsystem Technologies. 1–6
25. OptiFDTD Technical Background and Tutorials (Finite Difference Time Domain Photonics Simulation Software. https://www.optiwave.com, Accessed on 30th June, 2020
26. Garhwal A, Ray K, Arumona AE, Bharti GK, Amiri IS, Yupapin P (2020) Spin-wave generation using MZI embedded plasmonic antennas for quantum communications. Journal of Optical and Quantum Electronics 52(241):1–12
27. Wiesner K (2009) "Quantum cellular automata", In: Meyers R. (eds) Encyclopedia of complexity and systems science. Springer, New York
28. Arumona AE, Amiri IS, Punthawanunt S, Yupapin P (2020) High-density quantum bits generation using microring plasmonic antenna. Journal of Optical and Quantum Electronics 52(208):1–12
29. Arumona AE, Punthawanunt S, Ray K, Phunklang S, Yupapin P (2020) "Electron cloud spin generated by microring space-time control circuit for 3D quantum printing". Microwave and Optical Technology Letters. 1–7
30. Bunruangses M, Youplao P, Amiri IS, Pornsuwancharoen N, Yupapin P (2019) Brain sensor and communication model using plasmonic micrring antenna network. Opt Quant Electron 51(349):1–10
31. Bunruangses M, Sunat K, Mitatha S, Yupapin P (2010) Vehicular ad hoc network for a surveillance system using multifrequency band enhancement. Opt Eng 49(9):1–7
32. Babar S, Weaver JH (2015) Optical constants of Cu Ag and Au revisited. Appl Opt 54(3):477–481
33. Bahadoran M, Jalil MA, Ali J, Amiri IS, Yupapin P (2020) Realizing unique bifurcation model in a cascaded microring feedback circuit. Journal of Optical and Quantum Electronics 52(216):1–14
34. Pornsuwancharoen N et al (2017) Micro-current source generated by a WGM of light within a stacked silicon-graphene-Au waveguide. IEEE Photonics Technol Lett 29(21):1768–1771
35. Blaber MG, Arnold MD, Ford MJ (2009) Search for the ideal plasmonic nanoshell the effects of surface scattering and alternatives to gold and silver. J Phys Chem C 113:3041–3045
36. Chowdhury MZ, Hossan MT, Islam A, Jang YM (2018) A comparative survey of optical wireless technologies architectures and applications. IEEE Access 6:9819–9840
37. Pengnoo M et al (2020) Digital twin for metasurface reflector in 6G terahertz communications. IEEE Access 8:114580–114596